4D electrical resistivity tomography (ERT) for aquifer thermal energy storage monitoring

N. Lesparre, Tanguy Robert, Frederic Nguyen, Alistair Boyle, Thomas Hermans

4D electrical resistivity tomography (ERT) for aquifer thermal energy storage monitoring

Lesparre Nolwenn[1,2], Robert Tanguy [3,4,5], Nguyen Frédéric[1], Boyle Alistair[6], Hermans Thomas[1,4,7]

[1] Urban and Environmental Engineering, Applied Geophysics, Liege University, Quartier Polytech 1, Building B52/3, Allée de la découverte, 9, B-4000 Liege, Belgium, lesparre@unistra.fr, f.nguyen@uliege.be

[2] now at: Laboratoire d'Hydrologie et Géochimie de Strasbourg, University of Strasbourg/EOST/ENGEES, CNRS UMR 7517, 1 Rue Blessig, 67084 Strasbourg, France

[3] previously at: R&D Department, AQUALE SPRL, Rue Montellier 22, B-5380 Noville-les-Bois, Belgium

[4] F.R.S.-FNRS (Fonds de la Recherche Scientifique), Rue d'Egmont, 5, B-1000 Brussels, Belgium

[5] Urban and Environmental Engineering, Hydrogeology & Environmental Geology, Liege University, Quartier Polytech 1, Building B52/3, Allée de la découverte, 9, B-4000 Liege, tanguy.robert@uliege.be

[6] School of Electrical Engineering and Computer Science, University of Ottawa, 800 King Edward Avenue, Ottawa, Ontario, K1N 6N5, Canada, aboyle2@uottawa.ca

[7] Ghent University, Department of Geology, Krijgslaan 281, 9000 Ghent, Belgium, Thomas.Hermans@ugent.be

Abstract

In the context of aquifer thermal energy storage, we conducted a hydrogeophysical experiment emulating the functioning of a groundwater heat pump for heat storage into an aquifer. This experiment allowed the assessment of surface electrical resistivity tomography (ERT) ability to monitor the 3D development over time of the aquifer thermally affected zone. The resistivity images were converted into temperature. The images reliability was evaluated using synthetic tests and the temperature estimates were compared to direct temperature measurements. Results showed the capacity of surface ERT to characterize the thermal plume and to reveal the spatial variability of the aquifer hydraulic properties, not captured from borehole measurements. A simulation of the experiment was also performed using a groundwater flow and heat transport model calibrated with a larger set-up. Comparisons of the simulation with measurements highlighted the presence of smaller heterogeneities that strongly influenced the groundwater flow and heat transport.

Keywords: aquifer thermal energy storage, thermally affected zone, monitoring, electrical resistivity tomography, time-lapse, inversion

1 Introduction

The reduction of fossil fuel consumption is an objective for preserving non-renewable energy resources and reducing the impact of global warming. In this context, renewable and sustainable energies are promoted, e.g. Energy Efficiency Directive 2012/27/EU (European Council, 2012). Smart systems that use heat pumps to transfer heat to or from the ground can take advantage of the thermal stability of the subsurface to reduce energy consumption (Lo Russo et al., 2009; Vanhoudt et al., 2011; Sarbu and Sebarchievici, 2014). Beyond the different existing systems, ground source heat pumps present an inherent thermal resistance with boreholes, while groundwater heat pumps (GWHP) directly use groundwater that presents a relatively stable temperature over seasons. GWHP provide space heating or cooling, domestic hot water production, and are even used to store thermal energy, depending on the season and/or on the specific needs of the infrastructure (Allen and Milenic, 2003; Lo Russo and Civita, 2009). GWHP function through an open loop between two wells or groups of wells drilled in a shallow aquifer. During summer and/or any space cooling periods, water is extracted from the so-called cold well to cool down the infrastructure with the help of heat exchangers (geo-cooling). The thermal energy in excess, captured by heat exchangers, is then transferred to groundwater before its re-infiltration into the so-called warm well (Gringarten and Sauty, 1975; Ausseur et al., 1982; Voigt and Haefner, 1987). In winter, the GWHP functions in a reverse mode: water is pumped from the warm well and heat is transferred from groundwater to the building. Groundwater is then re-injected into the cold well with a lower temperature (Ausseur et al., 1982; Ampofo et al., 2006). Theoretically, the heat stored in the aquifer during space cooling periods allows an energy reduction for space heating and inversely with the cold stored during space heating periods for space cooling. Such systems are called aquifer thermal energy storage systems (Sommer et al., 2013, 2014; Bridger and Allen, 2014; Possemiers et al., 2015). GWHP working in shallow aquifers requires a relatively small ground surface area by comparison to ground source heat pumps. Thus the thermally affected zone (TAZ) is limited to a volume around boreholes (Sarbu and Sebarchievici, 2014). However, the induced temperature variations in the aquifer likely modify the medium properties such as the chemical composition and water quality (Bonte et al., 2013; Jesußek et al., 2013). Those changes might in turn impact the system efficiency but also the biodiversity, the microbial activities and consequently the ecosystem functions (Griebler et al., 2016).

In addition to controlling the temperature impact often imposed by regulations (Haehnlein et al., 2010), the design of GWHP requires a good understanding of the aquifer and heat flow conditions. In particular, issues of thermal short-circuit or recycling between cold and warm wells have to be carefully considered (Banks, 2009; Galgaro and Cultrera, 2013; Milnes and Perrochet, 2013). The propagation of the heat and cold plumes in the aquifer is also highly sensitive to possible variations of hydraulic gradient that could be induced by existing water wells and/or the drilling of additional wells close to the pumping system (Lo Russo et al., 2014) and to the heterogeneity of the subsurface (Bridger and Allen, 2014; Sommer et al., 2013, 2014; Possemiers et al., 2015; Hermans et al., 2018). Methods supplying insights on the heat or cold plume's propagation in the aquifer have to be developed, notably for delimiting the TAZ, to better anticipate the possible difficulties arising from GWHP implementation. Models of groundwater flow and heat transport are often calibrated with empirical values or from local measurements in boreholes (Lo Russo and Civita, 2009; Liang et al., 2011; de Paly et al., 2012; Mattsson et al., 2008; Raymond et al., 2011), ignoring the heterogeneity of the hydrogeological medium. Monitoring the 4D evolution of the TAZ through time is then particularly relevant. The relative proximity of the TAZ to the surface enables a monitoring with non-invasive geophysical methods (Hermans et al., 2014).

Electrical resistivity tomography (ERT) is particularly sensitive to the porous medium temperature (Rein et al., 2004; Revil et al., 1998; Hayley et al. 2007). Moreover, ERT applied in time-lapse (TL) provides spatially distributed information on the changes over time of the porous medium and may target salinity, water content or temperature (for a review on TL ERT see Singha et al., 2015). Thus, TL ERT is specifically appropriate to monitor heat plume development (Hermans et al., 2014). Acquisition systems can work autonomously, allowing the repeated measurements required to achieve sufficient temporal resolution to follow the 3D TAZ development. The method is also minimally invasive and requires low implementation costs compared to a dense network of boreholes. So far, the ability of ERT to monitor heat plumes has been demonstrated in 3D in a laboratory experiment at a scale of a few tens of centimeters (Giordano et al., 2016). Field 2D set-ups confirmed its relevance for monitoring heat storage, tracing experiments and borehole heat exchanger either from surface and/or cross-boreholes measurements (Hermans et al., 2012; Hermans et al., 2015; Giordano et al., 2017; Cultrera et al., 2017). However, 2D interpretation can be limited by out-of-the-plane or shadow effects during inversion which can limit the quantitative assessment of temperature (Nimmer et al., 2008). This effect is probably partly responsible for discrepancies observed between ERT-derived temperatures and direct cross-boreholes measurements by Hermans et al. (2015). The

use of 3D surveys and subsequent inversion can largely improve imaging of complex 3D subsurface objects (e.g., Van Hoorde et al., 2017).

In this paper, we image the development of the TAZ during a heat injection and storage experiment using a 3D ERT survey. The accuracy of ERT-derived temperature estimates is explored through synthetic cases that emphasize the method's sensitivity to target depth and thickness. Results show the ability of surface TL ERT to monitor the 3D development of the TAZ in a shallow aquifer. We compare our results with direct temperature measurements which demonstrates the ability of ERT to supply complementary insights about the sub-surface spatio-temporal dynamic. The ERT-derived temperatures show a general agreement with direct observations, **although important discrepancies are observed in the amplitude of the measured variations.** The latter are mainly explained by the different representative volumes of the two techniques **and the limitations related to the regularized ERT inversion**. A groundwater flow and heat transport model calibrated during a previous experimental set-up at a larger scale, is also computed. Its comparison with direct and ERT-derived temperature measurements underline the presence of local heterogeneities at the vicinity of the injection well which should be incorporated in the flow and transport model.

2 Field experiment

2.1 Hydrogeological context

The study site is located on the alluvial plain of the Meuse River at Hermalle-sous-Argenteau, 13 km north-east from Liège, Belgium. From borehole logs analysis, the subsurface medium can be divided into four lithological units. The first layer is composed of loam and presents a thickness of about 1 m. Below, the second unit is constituted of sandy loam, gravels and clay to a depth of 3 m. Between 3 and 10 m depth, the third layer is composed of gravel and pebbles in a sandy matrix. This third layer hosts the alluvial aquifer. It can be divided in two main units: the upper aquifer, between 3 and 6 m depth, composed of sandy gravels and the lower aquifer, between 6 and 10 m depth, characterized by coarser and cleaner gravels. The water table lies approximately at a depth of 3.2 m. Below 10 m depth, the basement of the aquifer consists of low permeability carboniferous shale and sandstone (Fig. 1).

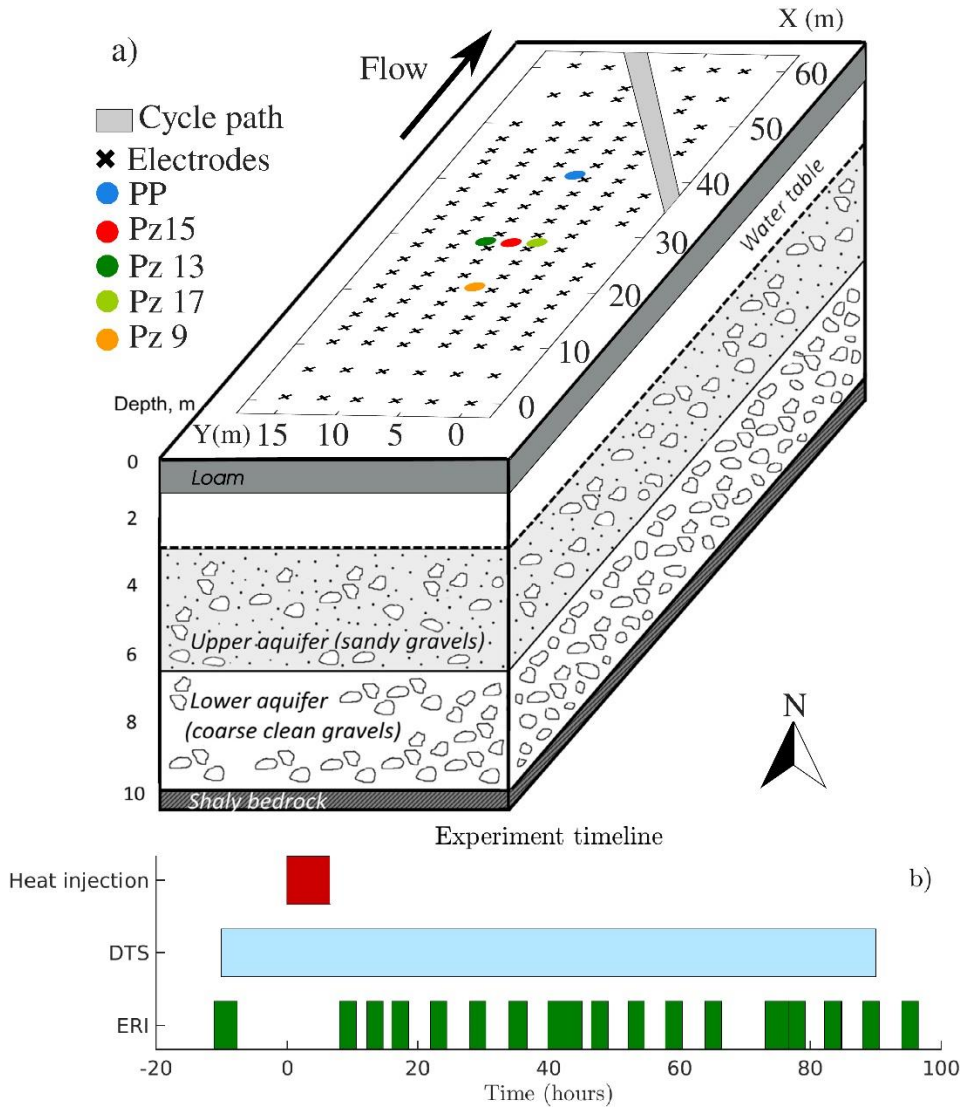

125 Figure 1: a) Scheme of the experimental set-up and structure of the underground medium (modified
126 from Klepikova et al., 2016). b) The experiment timeline shows the duration of the heat injection and
127 the DTS measurements as well as the moment of ERT acquisitions.
128
129 The site topography is almost flat and the natural hydraulic gradient in the aquifer is approximately
130 0.06% with a north-east direction (Brouyère, 2001). Previous experiments showed that the aquifer is
131 characterized by a high average permeability and by a horizontal and vertical heterogeneity
132 (Dassargues, 1997; Derouane and Dassargues, 1998; Brouyère, 2001). In particular, the upper and
133 the lower parts of the aquifer, ranging respectively in [3-6] m depth and [6-10] m depth present a
134 respective effective porosity of 4% and 8% as estimated from tracer test experiments (Brouyère,
135 2001). Direct measurements of Darcy fluxes were performed to estimate the groundwater flow
136 variations with depth. The lower part of the aquifer present Darcy fluxes in the range of [1-8]x10^{-3}
137 m/s, about one order of magnitude higher than in the upper layer where values range in [1-10]x10^{-4}
138 m/s (Wildemeersch et al., 2014). In a previous multiple tracer tests experiment, the monitoring of the

3D spreading of a heat plume resulting from the injection of heated water in the aquifer also showed lateral variations of the medium hydraulic properties (Klepikova et al., 2016), strengthened by 2D cross-borehole ERT and DTS measurements (Hermans et al., 2015). They confirmed the higher flow in the lower part of the aquifer and the lateral heterogeneity of the aquifer that presents zones of preferential flow (Hermans et al., 2015). Similarly, the thermal properties of the aquifer vary with depth as assessed during the ThermoMap project (Bertermann et al., 2013). The thermal conductivity was estimated at 1.37 and 1.86 W/mK and the volumetric heat capacity at 2.22 and 2.34 MJ/m³K in the layers located respectively at depths between 3 to 6 m and 6 to 10 m.

2.2 Heating and injection procedure

Water was pumped from the aquifer at the pumping well PP (Fig. 1a), its initial temperature was 13.4°C and the pumping flow rate was fixed to 3 m³/h. The water was then heated using a mobile water flow heater (Swingtec AQUAMOBIL DH6 system) before being re-injected with a flow rate of 3 m³/h. The heated water was injected in the borehole Pz 15 between 4.5 and 5.5 m depth (Fig. 1). Pz 15 is located in between two boreholes (Pz 13 and Pz 17) screened on the whole aquifer depth allowing DTS measurements (Fig. 1). The water was heated to a temperature of 42°C, i.e. with an increase of 28.6°C from the initial aquifer temperature. The hot water injection lasted 6 hours, but at the end of the injection step, water was injected at a temperature of 14.5°C during 20 minutes due to a technical issue with the water heater. Afterward, a heat storage phase lasted 4 days (Fig. 1b). The injected hot water volume is about 18m³ that can be used to estimate the order of magnitude of the heat plume development. The thermal plume can be assumed to develop in a 3 m height cylinder in the upper part of the aquifer that presents a porosity of 4%. Thus, the thermally affected zone should present a maximum volume of 450 m³ (ignoring conduction effects), developing in a cylinder of about 14 m diameter.

2.3 3D electrical resistivity data acquisition

Electrical resistivity measurements were performed from a grid of electrodes located at the surface to monitor the 3D heat plume evolution in the aquifer. 126 electrodes were placed along 6 profiles of 21 electrodes centered on the injection well and parallel to the natural flow direction (Fig. 1a). Along each profile the electrodes spacing was 2.5 m for the 17 central electrodes. Two electrodes at either end of each profile were spaced 5 m apart. That arrangement of electrodes was selected to allow a finer resolution around the injection well together with a greater penetration depth than profiles with equidistant electrodes. Some electrodes located on the northern side of the profiles 1 to 3 could not be hammered into the ground since the field is crossed by a concrete bike path. Thus, 1 or 2 electrodes were missing on those profiles (Fig. 1a). The electrode profiles were separated by 3 m so the electrode

grid covers the whole space available to image the plume without degrading the resolution perpendicular to the profiles. Data were acquired with gradient and dipole-dipole protocols along each profile (2D data acquisition). Cross-line measurements were also acquired (Van Hoorde et al., 2017), but ignored during inversion due to their low quality. We used an ABEM Terrameter LS connected to a relay switch ES10-64 allowing the acquisition in one shot of the whole data set for the entire electrode grid. A first data acquisition was performed the day before the heated water injection for reconstructing the background image. During the heat storage period 16 acquisitions were performed; once every six hours (Fig. 1b). For the background acquisition, reciprocal measurements were acquired for the whole data set to estimate the measurement error (LaBrecque et al., 1996). Reciprocal measurements correspond to a swap of the electrodes used for current injection and voltage measurements during the "normal" acquisition. A complete normal data set consisted in 3045 voltage measurements. For the time-lapse acquisition, the amount of reciprocal data was reduced to 1119 to speed up the acquisition. The acquisition delay was set to 0.3 s and the acquisition time was 0.5 s. The acquisition duration was 2.5 and 1.5 hours for the background and the time-lapse acquisitions, respectively.

2.4 Borehole measurements

Single-ended optical fibers were inserted in the Pz13 and Pz17 boreholes located on both side of the injection borehole (Fig. 1a). The optical fibers allow a direct monitoring of the temperature variations in the aquifer during the experiment, performed with an AP Sensing Linear Pro Series N4386. The distributed temperature sensing (DTS) measurements provide a spatial sampling of 0.2 m and a temporal resolution of 2 min. Since the aquifer vertical extension is relatively small (7 m) we choose to preserve the spatial resolution provided by the spatial sampling provided by the DTS. Instead, we preferred reducing the temporal resolution so we applied a running average through time over a 20 min window. Two sections of the optical fibers were placed respectively in a chilled and a warm water bath. The cold bath was maintained near 0°C (about 13°C cooler than the aquifer) by regularly adding ice. The baths' temperature was monitored with Pt100 sensors. The cable ends were placed at the bottom of the boreholes due to the small diameter of boreholes compared to the critical bend radius of optical fibers. Thus the differential attenuation of the light along the single-ended cables could not be estimated (Hausner et al., 2011). Nevertheless, the calibration baths allowed to correct the estimated temperatures, guaranteeing their temporal consistency throughout the experiment. DTS measurements were used for checking the relative temperature change ΔT from the initial state and not for an absolute monitoring of the aquifer temperature. The air temperature increased by 15°C at the end of the experiment. However, this effect is attenuated with depth and, although we can observe

a difference at a depth of 1 m in the DTS measurements, no temperature variation below 3 m (saturated zone) is visible.

3 Groundwater flow and heat transport model

3.1 Settings of the hydrogeological model

We used the 3D groundwater flow and heat transport model HydroGeoSphere (HGS) (Therrien et al., 2010) developed by Klepikova et al. (2016) for the Hermalle-sous-Argenteau experimental site to simulate numerically our experiment and compare temperatures derived from ERT and measured directly with DTS to the simulation. This deterministic model has been constructed and calibrated based on historical data (Dassargues, 1997; Derouane and Dassargues, 1998; Brouyère, 2001) and a multiple tracer experiment, including heat tracer (Wildemeersch et al., 2014; Hermans et al., 2015).

The model geometry corresponds to the one described by Klepikova et al. (2016), except that we refined the grid around the injection well to accurately model the experiment. In several aspects their experiment differs from the one presented here. They injected the heat tracer at the base of the Pz 9 borehole (Fig. 1a), so in the lower unit of the aquifer that is hydraulically more conductive. Furthermore, Pz 9 is screened over the whole thickness of the aquifer (Table 1) allowing heat propagation upward along the borehole. Their experimental design was adapted to constrain the hydraulic conductivity values on the whole aquifer section. In our experiment the temperature changes occurred in the upper part of the aquifer where heat was injected. Therefore, our data were more sensitive to the spatial variability of hydraulic conductivity distribution in the upper area. Moreover, they injected the heated water at a rate of 3 m^3/h during 24 hours and 20 minutes, while pumping at a constant discharge rate of 30 m^3/h in the pumping well (Fig. 1) in order to speed up the heat propagation in the aquifer. Therefore their experiment supplied information on the hydraulic properties in the whole domain in between the injection borehole Pz 9 and the pumping well (Fig1). In our case, we injected and stored the heat in the Pz 15 borehole so our experiment is more sensitive to hydraulic properties distribution in a smaller region surrounding that borehole.

Table 1: Main differences between the experiment of Klepikova et al. (2016) and the one presented in this study.

	This study	Klepikova et al., 2016
Depth of injection	5 m	9 m
Duration of injection	6 hours	24 hours and 20 minutes

Pumping time	Only during injection	All along the experiment
Pumping rate	3 m³/h	30 m³/h
Injection rate	3 m³/h	3 m³/h
Injection well	Pz 15	Pz 9
Injection well screen interval	-[5.5 ; 4.5] m	-[8.7 ; 3.2] m

The inversion process ran by Klepikova et al. (2016) sought the hydraulic conductivity distribution of the Hermalle site aquifer, in between the Pz 9 and the pumping well PP from a monitoring of the temperature changes in the upper and lower part of the aquifer from 11 observation boreholes. They estimated the hydraulic property values with the pilot point method to parametrize the inversion (Fig. 2). Here we use their resulting model to simulate the heat transport in the aquifer with the characteristics of our experiment. The model includes the density effects due to temperature changes (Graf and Therrien, 2005).

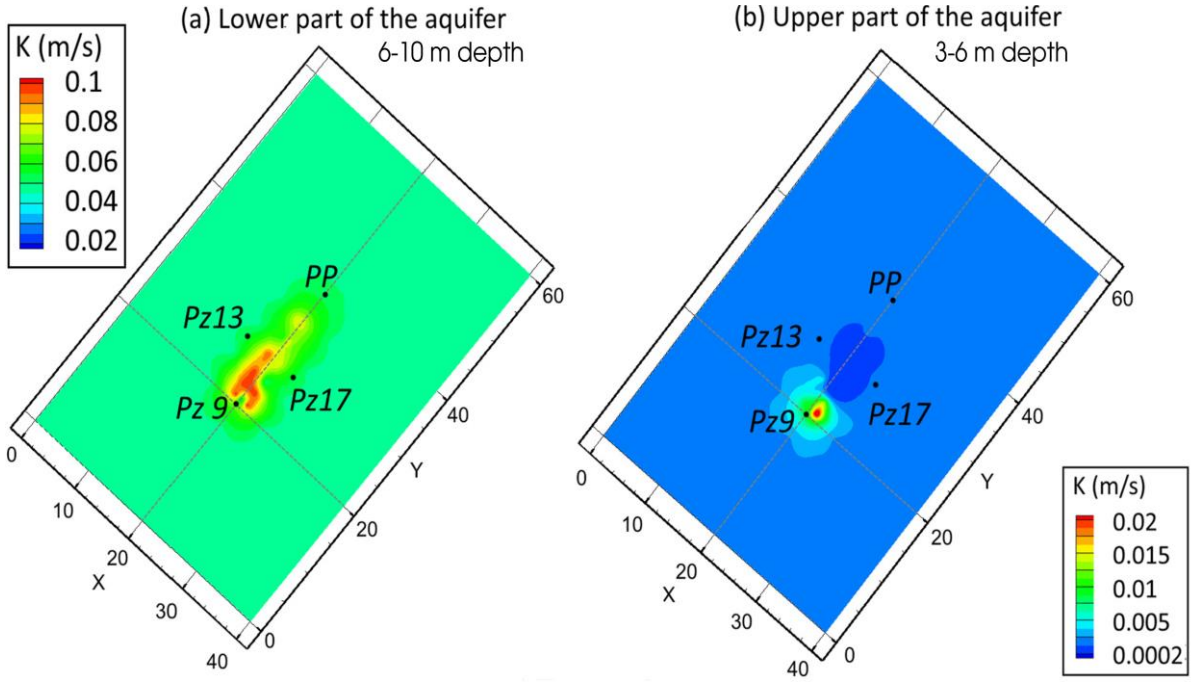

Figure 2: Spatial variability of the hydraulic conductivity K (m/s) models in XY planes for the lower (a) and upper (b) parts of the aquifer obtained from the inversion of transient temperature responses (Klepikova et al., 2016).

3.2 Temperature estimates from the HGS model

The temperature variations from the HGS model show a TAZ with a half-sphere geometry in the upper part of the aquifer (Fig. 3). In the lower part of the aquifer, the TAZ presents a tail along the X axis (towards NE which is the main flow direction; Fig. 3 c, d). The higher hydraulic conductivity

and the greater porosity in the lower part of the aquifer (Fig. 2 a) favors heat propagation with groundwater flow through convection. 8 h after the beginning of the injection, the diameter of the TAZ showing a ΔT of 4°C at a depth of 4.5 m is about 5 m and is slightly more elongated in the X direction. The lower diameter of the model TAZ compared to the above estimate for a cylinder of 14 m diameter can be explained by the fact that the model predicts a deeper propagation of the TAZ. Moreover, in the lower part of the aquifer the porosity is set higher in the model than the one used for the cylinder volume evaluation. 47 h after the injection started, the dimension of the model TAZ showing a ΔT of 4°C is slightly reduced to a diameter of about 3 m at a depth of 4.5 m. However at that time, ΔT in the middle of the TAZ is significantly lower, e.g. from 12°C after 8 h (Fig. 3 c) to 4°C for the same position after 47h (Fig. 3 d).

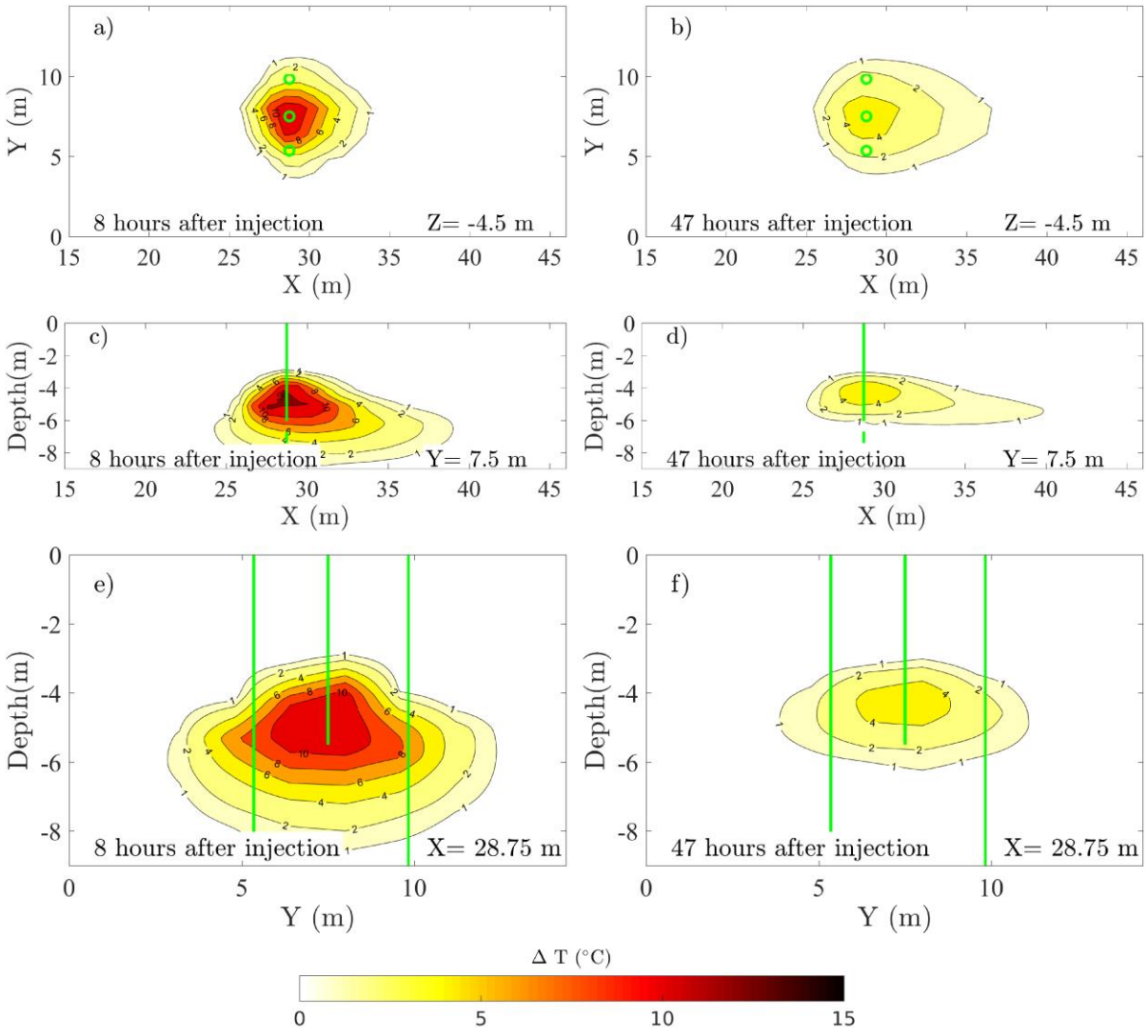

Figure 3: Temperature variation from the initial state estimated by the HydroGeoSphere model, 8 h and 47 h after the injection started on cross-sections in a horizontal layer at -4.5 m (a, b), on cross-section at the level of the injection borehole along the electrode profiles (c, d) and perpendicular to

the electrode profiles (e, f). The green circles and lines represent the injection and measurement boreholes. The black dotted lines and crosses correspond to the electrodes.

4 ERT-derived temperature images reconstruction process

4.1 Inversion method

The image reconstruction process in ERT aims to determine the spatial distribution of bulk resistivity in the medium that best reproduces the resistance measurements. An inverse problem is then solved to iteratively minimize the objective function $\Psi(m)$:

$$\Psi(m) = \Psi_d(d,m) + \lambda\Psi_m(m),$$

Equation 1

where $\Psi_d(d,m)$ measures the data misfit, $\Psi_m(m)$ defines model constraints for the inversion regularization and λ is the damping factor that balances the weight of the regularization. We used the EIDORS software for solving the inversion of the ERT data (Polydorides and Lionheart, 2002; Adler et al., 2015).

The data misfit $\Psi_d(d,m)$ is evaluated between observed measurements d (electrical resistances) and calculated data $f(m)$ computed from a model of resistivity m. Model and data are both expressed using their base 10 logarithm.

For the reconstruction of the medium background, before the introduction of perturbation through heat injection, the absolute values of the medium resistivity are sought and the data misfit is expressed as:

$$\Psi_d(d,m) = \sum_{i=1}^{N} \frac{|d_i - f_i(m)|^2}{|\epsilon_{B,i}|^2},$$

Equation 2

where ϵ_B are weighting factors accounting for the uncertainty of the measurements.

For time-lapse inversions, the inversion seeks the variations of resistivity from the background model. The measure of the data misfit is here defined using the difference between the background data d_{0i} (the subscript 0 refers to the background data) and the monitored data d_i:

$$\Psi_d(d,m) = \sum_{i=1}^{N} \frac{\left|(d_i - d_{0i}) - \left(f_i(m) - f_i(m_0)\right)\right|^2}{\left|\epsilon_{TL,i}\right|^2}$$

Equation 3

where m_0 stands for the model parameter distribution of the background state and ϵ_{TL} corresponds to the time-lapse data weighting.

The insertion of prior information on the medium structure is performed by $\Psi_m(m)$ in the inversion to stabilize the inverse problem:

$$\Psi_m = \left|\left|W_m(m - m_0)\right|\right|^2,$$

Equation 4

where W_m represents the regularization matrix that is here the identity matrix (Tikhonov, 1963). The background image m_0 was the result of a first inversion seeking the resistivity values of a medium constituted by four horizontal layers as highlighted by borehole logs analysis and previous ERT experiments (Hermans & Irving, 2017). The four layers correspond to a superficial unit above 1 m depth, below the unsaturated zone extends to 3 m depth, then to a depth of 10 m lies the aquifer over the bedrock. The depth of the interfaces are taken from borehole logs analysis. In the time-lapse reconstruction scheme, m_0 corresponds to the background image that refers to the initial state of the medium.

The computation of $f(m)$ is performed using a 3D finite element model built using the Netgen software (Schöberl, 1997). The unstructured mesh is refined close to the electrodes for a better accuracy of the resistance estimation, while elements are coarser further away from the electrodes allowing a reduced computation time. A regular coarse mesh was designed for the inversion in order to reduce the number of model parameters and thus stabilize the inversion procedure.

The inversion is performed using an iterative Gauss-Newton scheme and at each step a linear search against data misfit seeks the optimum value of the regularization parameter λ that minimizes the weighted residuals χ:

$$\chi = \sqrt{\frac{1}{N}\Psi_d(d, m)}.$$

Equation 5

The inversion is stopped either when the inversion converges, that is when further iteration do not provide a better data fit χ, i.e. no reduction of the objective function $\Psi(m)$ is observed, or when the desired misfit $\chi = |1 - \xi|$ is reached, with $\xi = 10^{-2}$. Such a stopping criteria avoids over-fitting data

and the presence of artefacts in the resulting image (Kemna, 2000). The data analysis and the method used to determine the error models weighting the data misfit are described in the appendix A.1.

4.2 ERT conversion to temperature images

Temperature variations in the aquifer induce a change of the medium electrical properties, i.e. the resistivity and its inverse the conductivity. The conductivity variations from the initial state and the temperature changes are related by a linear petrophysical relationship so temperature images can be derived from ERT (Hermans et al., 2014). We consider that bulk conductivity variations in the aquifer are due to changes of the fluid conductivity that depends on fluid salinity and temperature variations. We checked that chemical perturbations produced by temperature changes have a negligible effect on the fluid salinity (Hermans et al., 2015). Thus, the conductivity increase can be quantitatively interpreted in terms of temperature change using the linear relationship:

$$\frac{\sigma_{f,T}}{\sigma_{f,25}} = m_f(T - 25) + 1$$

Equation 6

where $\sigma_{f,T}$ stands for the fluid conductivity at a temperature T and m_f corresponds to the fractional change of the fluid conductivity per degree Celsius around the reference temperature $T = 25°C$. From water samples taken on site the trend between the temperature and the fluid conductivity was estimated to be $m_f = 0.0194$ and the fluid conductivity at $T = 25°C$ was evaluated at $\sigma_{f,25} = 0.0791\, S/m$ (Hermans et al., 2015).

Temperature change from the initial state ΔT images can be constructed from the observed variations of the bulk conductivity σ_b by converting them with (Hermans et al., 2014; 2015):

$$\Delta T = \frac{1}{m_f}\left(\frac{\sigma_{b,TL}}{\sigma_{b,B}}\frac{\sigma_{f,B}}{\sigma_{f,25}} - 1\right) + 25 - T_{init}$$

Equation 7

$\sigma_{b,B}$ and $\sigma_{b,TL}$ correspond respectively to the bulk conductivity of the background state and of a time-lapse acquisition. $\sigma_{f,B} = 0.0614\, S/m$ represents the fluid conductivity at the initial state and was estimated from Eq. (6) with an initial temperature of $T_{init} = 13.44°C$. That initial temperature value corresponds to the average of the temperatures measured along both boreholes using DTS before the heat injection. The estimate of the initial conductivity of the fluid was validated with a value of $\sigma_{f,B} = 0.0598\, S/m$ by direct measurement with a CTD probe in the injection borehole.

4.3 Sensitivity analysis of the ERT-derived temperature images

We ran synthetic simulations computed from models of a cylindrical plume with different thicknesses and positions in the aquifer in order to evaluate the sensitivity of the electrode array to the target depth and thickness. The temperature increase in the cylinder was fixed to 17°C and the cylinder diameter to 8 m based on the outcomes of the HGS model. The cylinder was centered on the injection borehole Pz 15 (Fig. 1). The tested cylinder heights varied between 1.5 m and 5 m. The cylinder upper limit positions checked was of -3 m and - 4 m so it is always located below the unsaturated zone (Fig. 4). On all images, we observe that the inversion allows a fairly correct reconstruction of the target shape when the target is located close enough to the electrodes (approximately the distance corresponding to the electrode spacing) or sufficiently thick to be detectable (at least the electrode spacing). We note that the target upper limit is always overestimated by about 2 m and that the amplitude of ΔT decreases with depth. The region of higher ΔT in the reconstructed target is also shifted upward the center of the actual target. Moreover, the temperature increase leaks out of the synthetic target delimitation, except in the shallow region where artifacts induce a reduction of the electrical conductivity (Fig. 4). Quantitatively we can compare the estimated temperature increase at the level of the injection borehole Pz15 to the synthetic target as summarized in Table 2. We note that when the target is relatively shallow, that is for an upper limit at -3 m, the increase of the target thickness greatly helps determining more closely the target true temperature. However if the target is only 1 m deeper, the target thickness increase does not allow accurate estimates of the target temperature.

Table 2: Percentage of the temperature increase estimated by ERT from the synthetic target increase for different cylinder height and upper position.

Height \ Upper limit	1.5 m	2.5 m	4 m	5 m
-3 m	24 %	44 %	67 %	78 %
-4 m	17 %	30 %	41 %	46 %

The target blur and the global temperature underestimation are related to the regularization that favors a smooth change from the background model. The smoothing effect hinders a precise location of the target and thus an overestimation of the target depth. Moreover, the estimation of ΔT at depth is degraded by the reduction of the ERT sensitivity with depth (Fig. 4). From those tests, we infer that the geometry of the plume (its size and depth) is fairly estimated, with an overestimation of the plume vertical position when the target depth and thickness correspond to the electrode inter-distances. Furthermore, images underestimate the actual temperature changes in the aquifer. Smoothing effects

and the underestimation of the aquifer parameters using TL-ERT are well known and results from the regularization procedure in the inversion (Singha and Moysey, 2006).

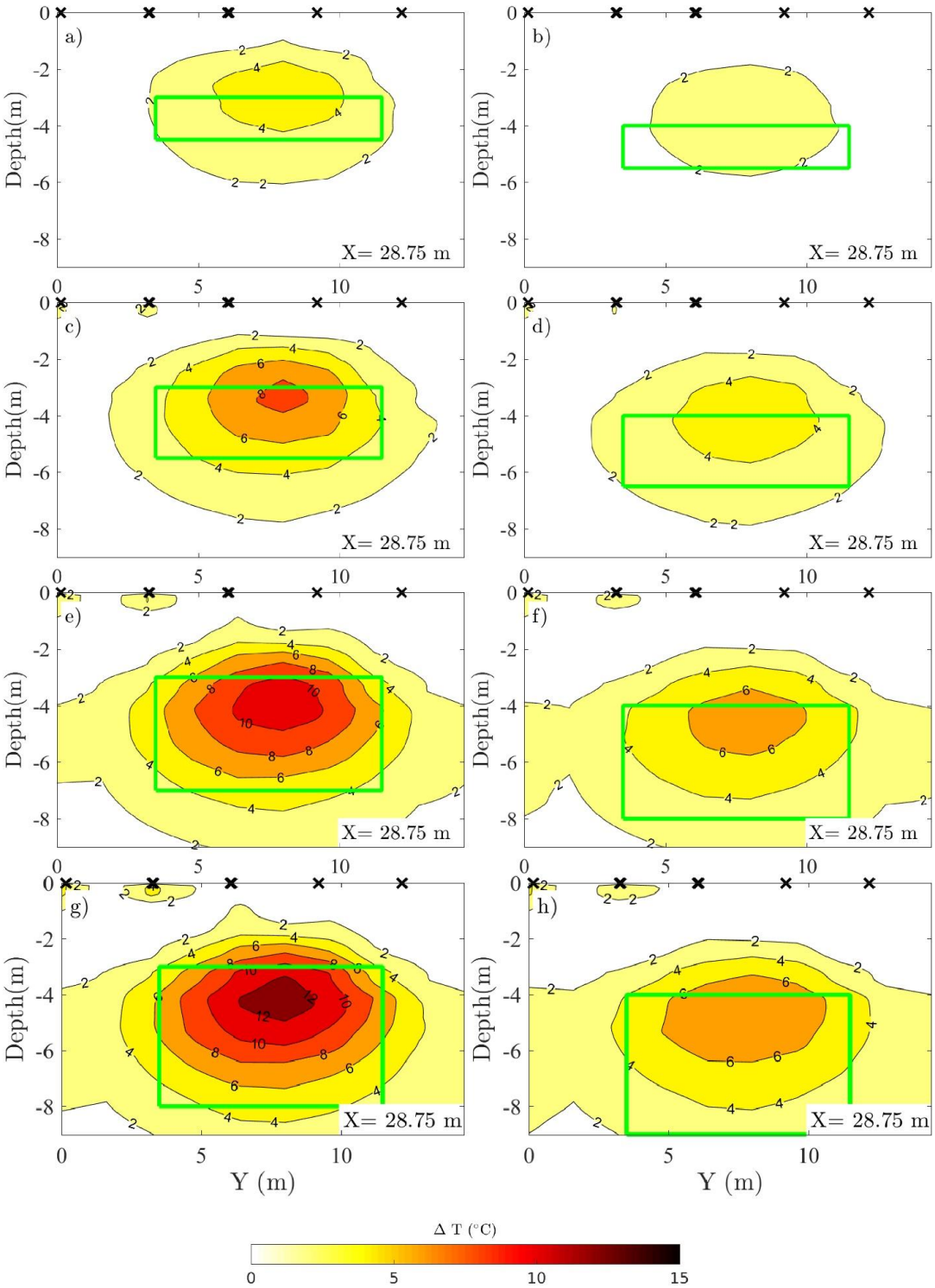

Figure 4: Temperature variation estimates from synthetics built as a vertical cylindrical heat plume. The cylinder thickness is of 1.5 (a, b), 2.5 (c, d), 4 (e, f) and 5 m (g, h) and its upper limit is at -3 m (a, c, e, g) and -4 m (b, d, f, h). The green lines indicate the shape of the cylindrical target, the black crosses correspond to the electrodes.

5 Results from field data

5.1 Background images

The 3D inversion of the background ERT data set provides the distribution of the subsurface resistivity with a root mean square of the data misfit of 1.03%. The results are presented by 2D vertical cross-sections corresponding to each acquisition profile (Fig. 5). The images show the vertical variations of the electrical resistivity corresponding to the four lithological units. The superficial conductive layer with a thickness of 1 m and a resistivity of about 115 Ω.m corresponds to the loam unit. Between 1 and 3 m deep the medium presents heterogeneous variations of resistivity with zones of a few meters length showing a resistivity higher than 400 Ω.m and locally values reaching 1000 Ω.m while the surrounding medium presents a resistivity of 250 Ω.m. Here the resistive regions might be interpreted by lenses of clean unsaturated gravels in a medium of sandy loam and gravels. Below, in the aquifer layer at a depth between 3 and 10 m the medium presents a median resistivity of 180 Ω.m with some more conductive areas notably below profiles located on Y= 6 and 9 m where the resistivity is around 100 Ω.m. Those conductive anomalies are likely an effect of the pumping well metallic-casing. We note that we do not distinguish any clear resistivity variations related to the different nature of the aquifer upper and lower units. Previous ERT experiments discriminated between the upper and lower regions through a higher resolution cross-borehole survey (Hermans et al., 2015), or through a specific analysis developed for discriminating the different facies of the medium (Hermans and Irving, 2017), which were not used in this study. Finally, the lower layer located below 10 m depth in the bedrock shows a median resistivity of 280 Ω.m. Those values are in accordance with previous ERT investigations on the site (Hermans and Irving, 2017).

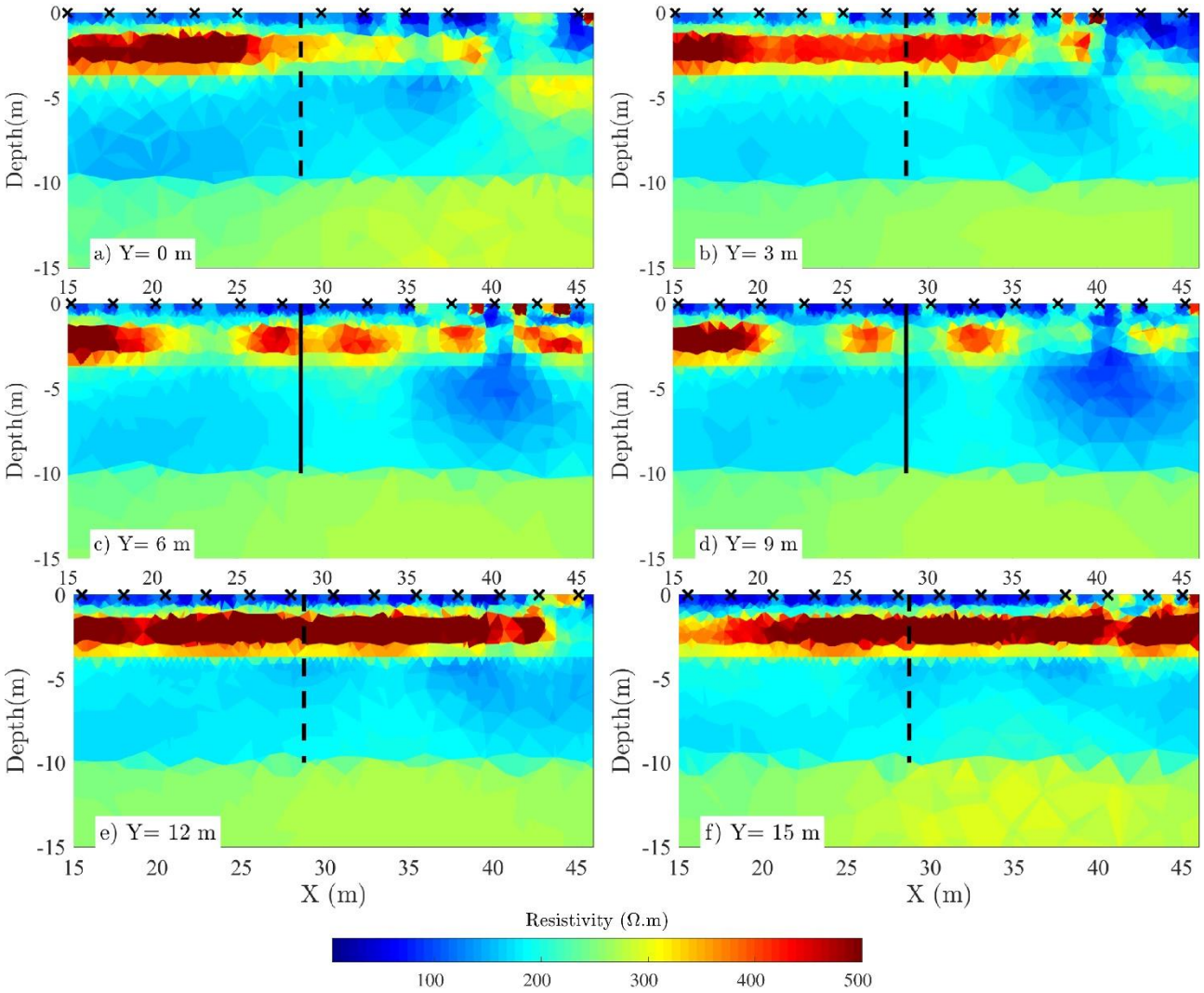

412 Figure 5: Electrical resistivity cross-sections extracted below each electrode profile from the 3D
413 model. The black hashed or solid lines represent the injection and measurement boreholes projection.
414 The black crosses correspond to the electrodes.

415

416 ## 5.2 Time-lapse conductivity variation images

417 Since conductivity variations vary linearly with temperature we choose to represent that property
418 instead of resistivity variations over selected time steps (8 h and 47 h after the injection started) on
419 sections of the 3D model (Fig. 6). A conductive plume, with a variation between 10 and 30% from
420 the initial state, is observed in the upper part of the aquifer (Fig. 6c to f). The region showing a
421 conductivity increase higher than 10% presents an oval geometry with a horizontal extent of about
422 5 m along the X axis and 10 m in the Y direction (Fig. 6a and b). The plume is not centered on the
423 injection borehole, but is slightly shifted along the X axis, in the same direction as the natural
424 groundwater flow. The region with the highest conductivity change is also slightly shifted in the Y
425 direction. The global shape of the zone affected by conductivity changes does not significantly evolve
426 with time, but the conductivity further increases more than 50 hours after the end of the injection. A

second conductive target is observed at Y=0 m, below the first profile which is lacking central electrodes. We interpret this more conductive zone as an artifact related to a lower sensitivity in that region due to the missing electrodes (Fig. 6). The images also present regions with a conductivity decrease from the initial state, mostly in the shallow region but also at depth below profile 1 and at the extremity of the central profiles. In the shallow region, they might be related to changes in the medium saturation above the aquifer. Below, we interpret them as artifacts that are strengthened by our less conservative choice of error model (see Appendix A.1).

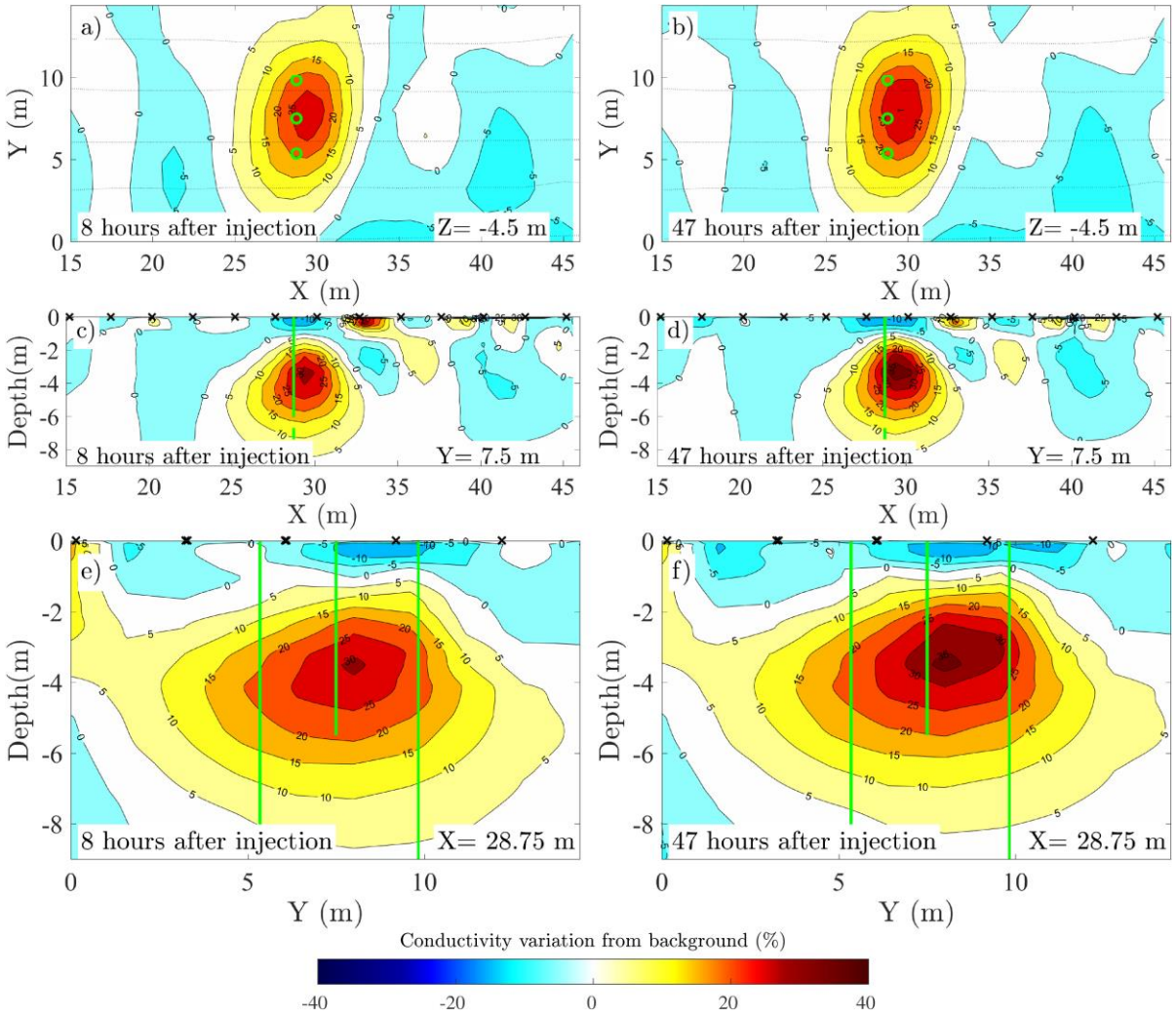

Figure 6: Conductivity variations 8 h and 47 h after the injection started with respect to the background measurements in a horizontal layer at -4.5 m (a, b), on cross-section at the level of the injection borehole along the electrode profiles (c, d) and perpendicular to the electrode profiles (e, f). The green circles and lines represent the injection and measurement boreholes. The black dotted lines and crosses correspond to the electrodes.

5.3 ERT-derived temperature images

ERT-derived ΔT images show a similar shape and evolution of the TAZ as the conductivity variation images (Fig. 7). On those images, ΔT is fixed to 0°C in regions showing negative contrasts of conductivity since we interpret them as artifacts. The TAZ with a ΔT increase of 4°C from the initial state presents an oval shape in the horizontal plane at Z=-4.5 m with a length of 10 m in the Y direction and a width of 5 m along the X axis (Fig. 7a, b). As on the conductivity variation images, the shift along the X and Y directions of the TAZ with a highest ΔT is observed (Fig. 7c, d, e, f). From the synthetic tests, we deduce that the TAZ oval shape is not an effect of the electrode design or inversion, but reflects the actual shape of the TAZ. This highlights the usefulness of ERT in providing information on the plume anisotropy. ERT-derived ΔT images show a relatively shallow TAZ upper limit, in the region where the method sensitivity is still adequate for detection. However, as observed from the synthetic inversions, the TAZ upper limit deduced from ERT might be overestimated by 2 m. The TAZ should indeed be confined below the water table (3 m depth, Fig. 1). Similarly to the synthetic cases, it is difficult to properly image the shape of the TAZ in the lower part of the aquifer from ERT inversions, due to the low sensitivity (Fig. 4). Quantitatively, 8 hours after the beginning of injection, the derived ΔT reaches locally 12°C in the upper part of the aquifer between the injection borehole and the electrode profile at Y=9 m (Fig. 7). 40 hours later, that region shows a higher ΔT value of 14°C. However, a difference of only 2°C is in the range of uncertainty observed in the synthetic tests, it is thus difficult to confirm this 2°C increase. Nevertheless, we note the persistence of a TAZ on the ERT-derived ΔT images with a similar shape 8 h and 47 h after the injection (Fig. 7).

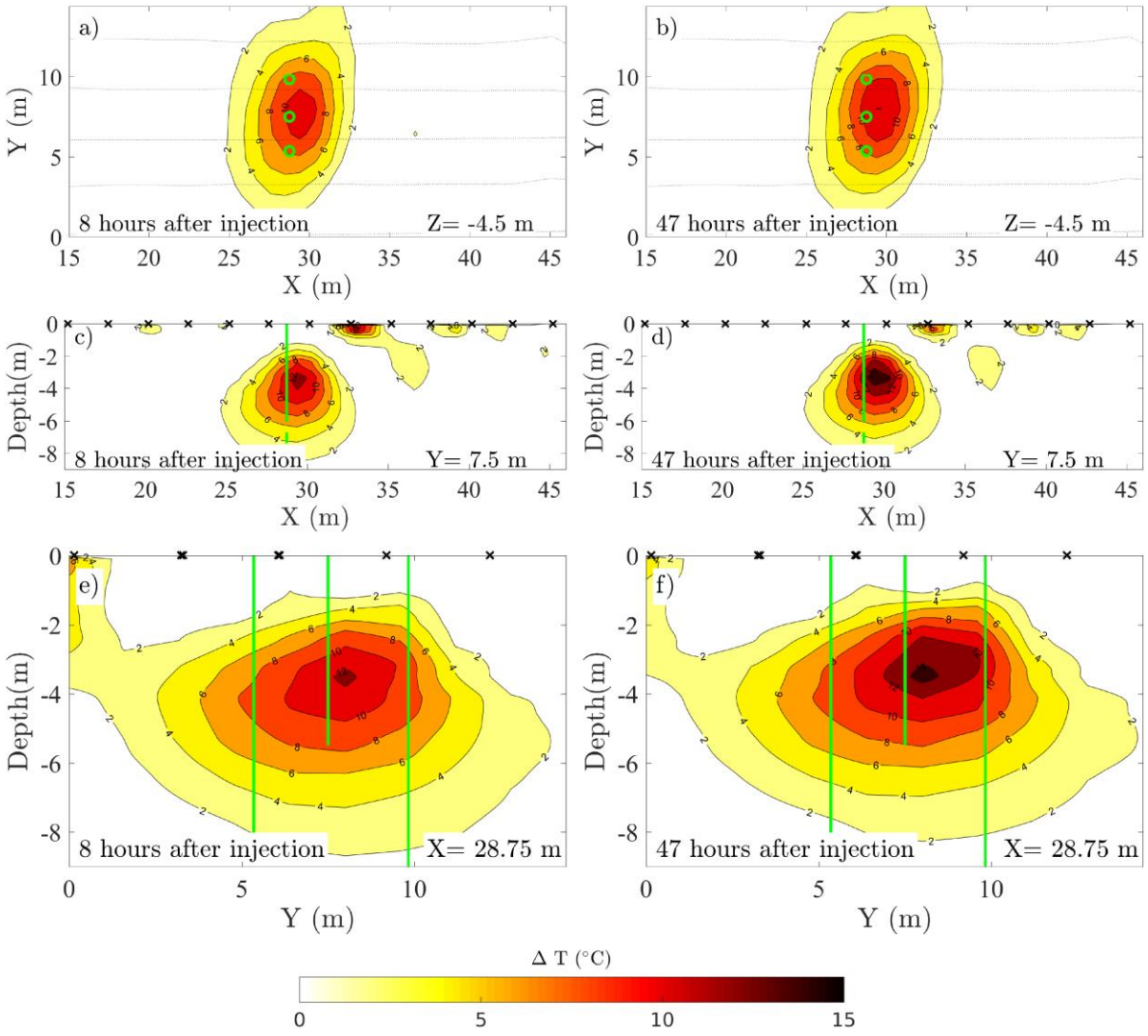

462 Figure 7: Temperature variation from the initial state estimated from ERT 8 h and 47 h after the
463 injection started in a horizontal layer at -4.5 m (a, b), on cross-section at the level of the injection
464 borehole along the electrode profiles (c, d) and perpendicular to the electrode profiles (e, f). The green
465 circles and lines represent the injection and measurement boreholes. The black dotted lines and
466 crosses correspond to the electrodes.
467
468 Predictions from the HGS model and ERT-derived ΔT results are represented on cross-sections to
469 ease their comparison (Fig. 8). The edges correspond to the TAZ showing a ΔT of 4°C from the initial
470 state, at different times after the injection. Estimates derived from ERT show a coarser TAZ with a
471 shape preserved all along the experiment, probably due to the smoothing effect of the inversion as
472 demonstrated by the synthetic tests. They illustrate the gradual plume shift along the X and Y
473 directions. Predictions from the HGS model show a smaller TAZ confined at the level of the hot water
474 injection. The dimension of the predicted TAZ shrinks progressively and vanishes after 58 h.
475 Compared to ERT-derived ΔTcontours, the HGS predictions show also a stronger influence of the

natural groundwater flow that transports the plume in the X direction, notably in the lower part of the aquifer. Note that the natural flow was estimated from a regional model (Brouyère, 2001) and has a larger influence in our experiment than in the one used for calibration given the lower pumping rate (Table 1). Finally, the HGS predicted plumes do not show the significant anisotropy with an elongation in the Y direction in the horizontal plane observed on the ERT results.

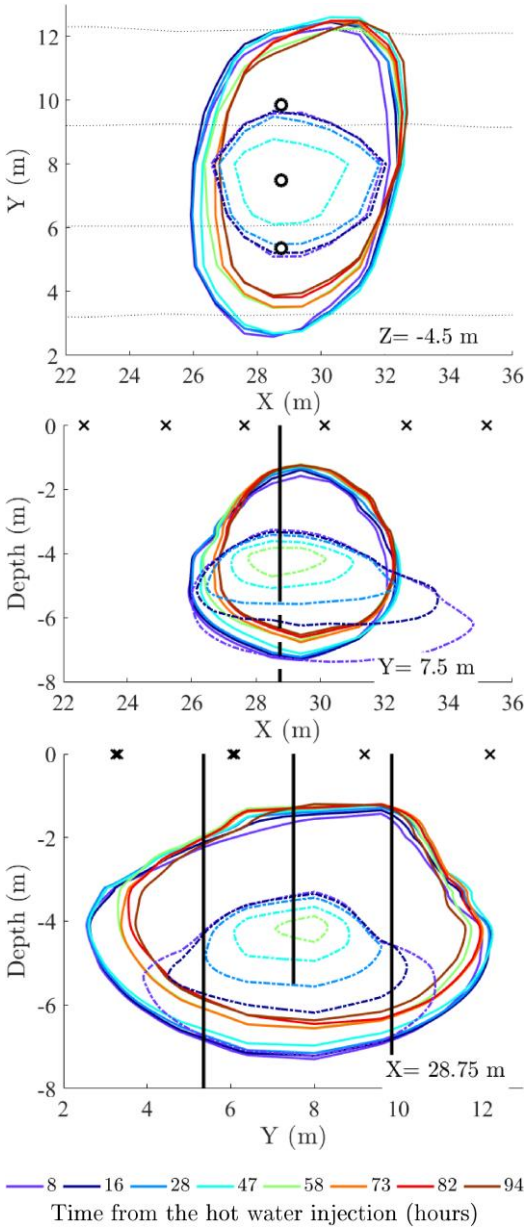

Figure 8: Evolution of the plume shape over time, with a contour line at ΔT = 4°C. The colored lines represent estimates from ERT and the hashed colored lines predictions from the HGS model. Data are presented on cross-sections in a horizontal layer at -4.5 m (a), at the level of the injection borehole along the electrode profiles (b) and perpendicular to the electrode profiles (c). The black circles (a) and lines (b,c) represent the injection and measurement boreholes. The black dotted lines (a) and crosses (b,c) correspond to the electrodes.

5.4 Direct temperature measurements

DTS direct temperature measurements in the aquifer show that the temperature variation from the initial state ΔT reaches 20°C in the upper part of the aquifer, while in the lower part ΔT is about 10°C with a local increase to 15°C (Fig. 9). From the end of the injection, ΔT decreases abruptly at depth below 5 m, while in the upper part ΔT decreases gradually with time. We also note that measurements performed at Y=9.85 m show a larger and stronger print of the TAZ than measurements performed at Y=5.35 m. Thus DTS measurements confirm the plume shift in the Y direction observed from ERT. During the injection, the heat plume propagates at depth until the bottom of the boreholes (Fig. 9). However, the heat increase in depth might be related to local convection around boreholes and not due to heat propagation through the whole aquifer (Hermans et al., 2015; Klepikova et al., 2016).

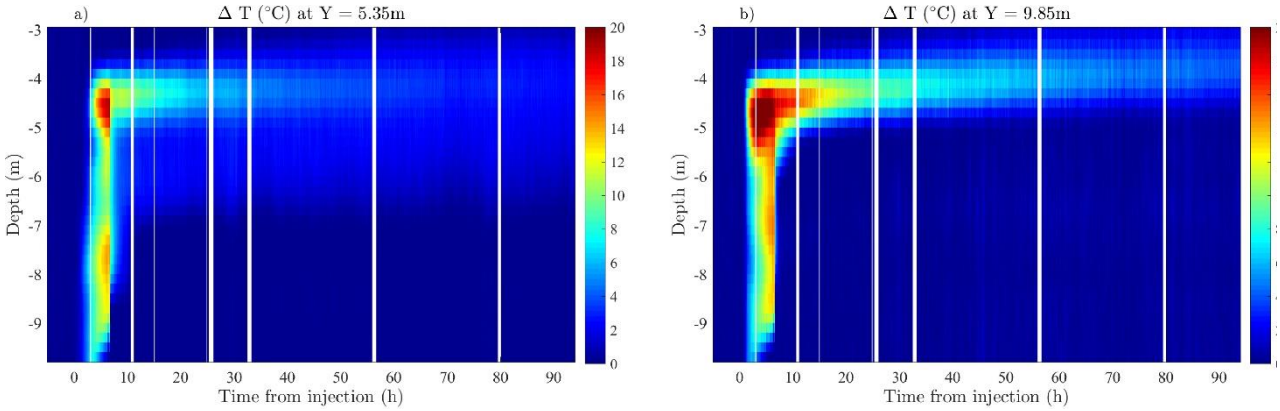

Figure 9: Temperature variation from the initial state estimated with the DTS all along the aquifer section at the measurement boreholes Pz17 (a) and Pz13 (b).

5.5 Comparison of temperature dynamics

The dynamics of ΔT from direct measurements, ERT estimates and the HGS predictions are compared at the level of the measurement and injection boreholes (Pz 13, 15, 17 Fig. 1) at a depth of 4.5 m (Fig. 10). That depth corresponds to the highest temperature measured with DTS (Fig. 9). Direct ΔT measurements are acquired using DTS data for Pz 13 and Pz 17 and a CTD probe for the injection borehole Pz 15 (Fig. 1). ERT-derived ΔT estimates correspond to values extracted from the voxels of the 3D models obtained by the inversion of each data sets acquired after the hot water injection. Similarly, predictions correspond to values extracted from the HGS model voxels at different simulation times.

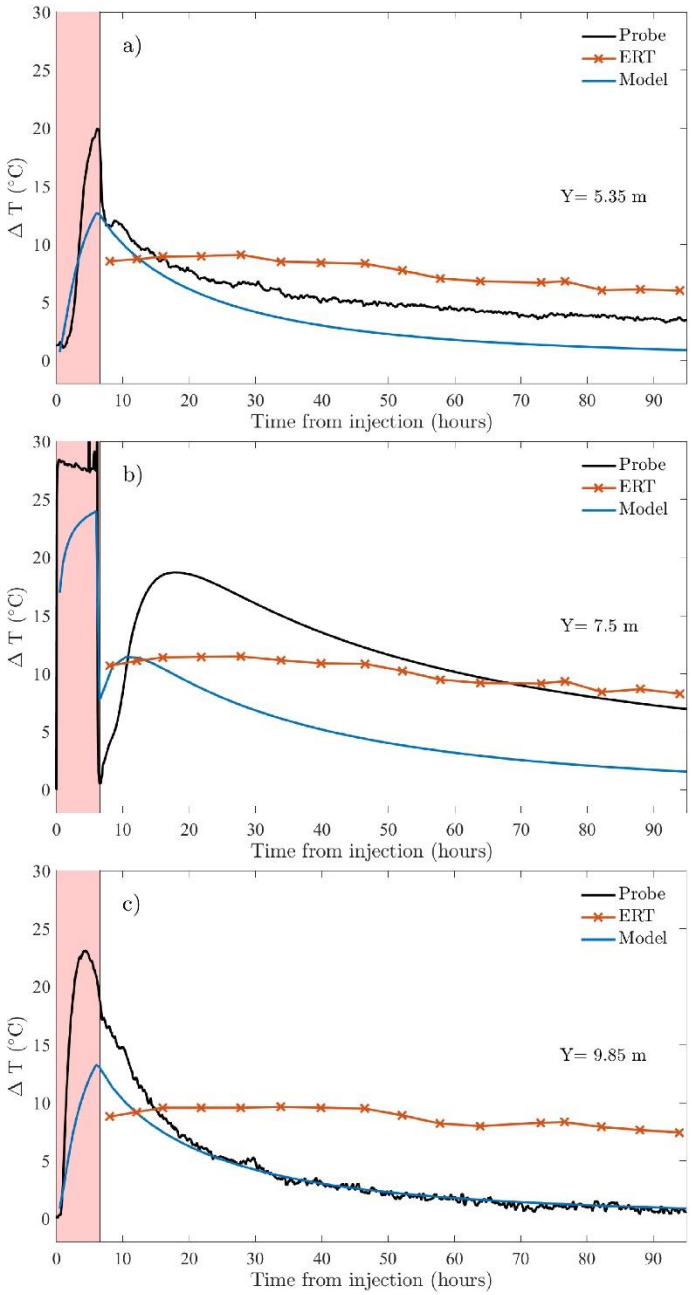

Figure 10: Temperature variations from the initial state at a depth of 4.5 m at the level of Y=5.35 m (a), Y=7.5 m (injection borehole), b) and Y=9.85 m (c). The red zone represents the duration of the heat injection. ERT estimates are obtained from the 3D time-lapse inversions. Model predictions were computed with the HGS model.

The probe located in the injection well (Y=7.5 m, Fig. 10b) shows an average ΔT value of 27°C during the injection phase. Then ΔT decreases sharply to 0.5°C and softly increases to a peak value of 19°C due to the injection of cold water. ΔT decreases then gradually to a value of 7°C at the end of the experiment. Those direct measurements confirm the persistence of the TAZ all along the experiment as observed with ERT (Fig. 7, 8, 10). DTS measurements in neighboring wells do not show the same rebound pattern but instead a faster ΔT decrease at the end of the injection phase. In

the measurement borehole at Y=5.35 m, direct ΔT measurements reach 20°C during the injection phase and decrease to 3.5°C at the end of the experiment (Fig. 10a). The second measurement borehole at Y=9.85 m shows a different dynamic with a higher ΔT value that reaches 23°C during the injection phase but decreases to a lower value of 0.5°C at the end of the experiment (Fig. 10c).

ERT-derived ΔT clearly miss to capture the dynamics of the temperature decrease within the TAZ. ΔT values are underestimated a few hours after the injection phase and overestimated later (Fig. 10). In general, all ΔT curves derived from ERT are rather stable, although showing a slight decreasing trend, compared to the direct ΔT measurements. In particular ERT–derived ΔT remains higher at the end of the experiment (ΔT of 6°C and 7.5°C in borehole at Y=5.35 m and Y=9.85 m respectively, Fig. 10). Those observations confirm the results of the synthetic tests, showing that the survey design is mostly sensitive to the global temperature change around the well.

The comparison of the HGS model prediction with the ΔT direct measurements shows that the model globally underestimates ΔT values compared to direct measurements (Fig. 10). The HGS model predicts lower ΔT values at the end of the injection phase in the three boreholes of 12.5°C, 24°C and 13.5°C for a Y position of 5.35, 7.5 and 9.85 m respectively (Fig. 10a). At the end of the experiment the HGS model predicts a ΔT value of 1.5°C in the injection borehole, confirming its inability to represent the TAZ persistence. At that time, in both measurement boreholes show similar ΔT values of about 1°C.

6 Discussion

The experiment performed here demonstrates the capacity of ERT to deliver useful information about the 4D evolution of a thermal plume in a shallow aquifer. ERT-derived ΔT images supply information on the plume anisotropy in a horizontal plane and its persistence all along the experiment (Fig. 7, 8, 10). The plume anisotropy is attested with synthetic tests but cannot be deduced from direct measurements as boreholes close to the injection well are lacking along the X axis. However, direct measurements in the injection well confirm the TAZ persistence through time (Fig. 10b). So the performed experiment provides an interesting insight on the aquifer storage heat capacity not expected by the HGS model. The revealed anisotropy in the XY direction by ERT might indicate the presence of a preferential water flow path bypassing hydraulic barriers. Such a preferential flow path in the upper part of the aquifer can be related to clay lenses channeling groundwater flow in the Y direction. Despite TL ERT supplying smoothed results due to regularization, the method has the capacity to provide useful insights about local hydraulic conductivity heterogeneity. The suspected

554 local heterogeneities have a strong influence on the groundwater flow and hence on heat transport.
555 However, those small heterogeneities are not taken into account in the existing HGS model. The
556 hydraulic parameters used for the simulation should be adjusted around the injection well to
557 reproduce the plume evolution. Indeed, the hydraulic parameters were determined during a previous
558 experiment representative of a larger scale. The integration of hydraulic parameter variations at that
559 smaller scale into the model could help reproducing the horizontal anisotropy of the TAZ
560 development revealed by ERT.
561
562 **In this specific experiment, although ERT identifies the trend, it does not accurately identify**
563 **the temporal fluctuations of** ΔT. Indeed, DTS measurements show a significant ΔT decrease in both
564 monitored boreholes, while ERT only indicates a slight decreasing trend (Fig. 10). **The agreement**
565 **is better in the injection well.** Such examples illustrate the difficulty in comparing data
566 representative of ΔTchanges in different volumes. On the one hand, heat loss towards the atmosphere
567 might have favored the ΔT decrease observed with DTS within wells. On the other hand, since ERT
568 acquisitions are sensitive to temperature changes in a large volume, their estimates might better reflect
569 the matrix heat storage and release. DTS and CTD measurements are bathed in the borehole water
570 and thus not directly connected to the conditions in the aquifer. **In addition, the injection of**
571 **unwanted cold water further complicated the distribution of temperature in the aquifer,**
572 **creating an anomaly below the resolution of ERT.**
573
574 Quantitatively, the ability of ERT to image the dynamics compared to direct measurements is also
575 limited since we note an underestimation of ERT-derived ΔT values a few hours after the injection
576 phase and an overestimation later. This is a direct consequence of the regularization, as highlighted
577 by the synthetic inversions (Singha and Moysey, 2006). **In practice, a small plume with high**
578 **temperature yields the same image as a large plume with a lower temperature. Combined with**
579 **the slow dynamic characteristic of a storage experiment, it generates ERT images with limited**
580 **amplitude variations, but with the correct trend.**
581
582 Due to regularization, ERT-derived ΔT images also present a shift in the vertical position of the plume
583 and a coarse shape of the TAZ, both identified with synthetic tests. The effect of blur could be
584 attenuated by reducing the acquisition time, by acquiring a limited amount of reciprocal data (Rucker,
585 2014). Other regularization method such as covariance constraints or minimum-gradient support
586 might help overcome the smoothing effect and improve the delineation of the TAZ (Hermans et al.,
587 2016b; Fiandaca et al., 2015; Nguyen et al., 2016). Furthermore, ERT lacks sensitivity in the

horizontal dimension due to the electrode inter-distance and the volume integrative sounding of the method. Observed changes with ERT are therefore representative of an average temperature variation in a 3D volume that prevents the reconstruction of an accurate TAZ shape and temperature estimate. The decrease of the ERT sensitivity with depth also hinders delimiting precisely the TAZ in the deeper region. This is further complicated due to the higher groundwater flux easing the plume transport as shown in the HGS model and DTS measurements (Fig. 2, 3, 9).

Discrepancy with direct measurements, providing local information of the medium properties surrounding the boreholes might be partly explained by perturbations in water circulation related to boreholes drilling and screening. Indeed, we suspect that strong temperature variations observed in the lower part of the aquifer during the hot water injection might be due to internal flow (Fig. 9). The integrative nature of ERT might also affect the comparison with local measurements. The latter, coupled to the adverse effects of inversion also hinders ERT-derived ΔT images to reflect properly the TAZ dynamic. However, beyond the production of ERT-derived ΔT images, discrepancies in the sensitivity of ERT and DTS could be exploited to better constrain hydraulic properties of the aquifer close to the injection borehole, considering they supply complementary insights on the medium properties. The information about the TAZ shape development from ERT can help conceptualizing the spatial variability of hydraulic properties in the aquifer, while direct measurements furnish a quantitative estimate of the temperature variations. So coupled inversion fitting simultaneously the surface resistance measurements and the direct temperature acquisitions is worth considering to evaluate accurately the TAZ location and geometry (Pollock and Cirpka, 2012). The coupled inversion would remove the regularization smoothing and would help refining the hydraulic property distribution around the injection well, which strongly affects predictions. Alternatively, the set-up of a stochastic inversion by model falsification such as a prediction focused approach would also benefit from the complementary nature of ERT and DTS data (Hermans et al., 2016a, 2018). Such a methodology presents the advantage that the developed analysis directly focuses on the prediction of the TAZ with the different measurement types, also avoiding any regularization.

7 Conclusion

Although a quantitative estimation of temperature was not possible in this experiment, due to the inherent limitations of inversion, our study demonstrates the pertinence of the minimally invasive 4D ERT method to provide qualitative, complementary insights on the development of a thermal plume in a shallow aquifer. The ERT-derived ΔT images obtained here inform about the anisotropic shape of the thermal plume and its persistence all along the experiment. Hence, the method indicates the

presence of local heterogeneities at the vicinity of the injection well and the aquifer heat storage capacity confirmed by direct measurements. The anisotropic behavior cannot be validated using direct temperature measurements as it would have required a denser network of boreholes close to the injection well (Fig. 1). Thus, ERT measurements provide crucial information for the set-up of groundwater heat pumps (GWHP), which requires an accurate knowledge of the spatial variability of the aquifer's hydraulic and heat capacity properties. So, the insertion of a correct distribution of the hydraulic properties in the hydrogeological model has to be performed for estimating the likely shape and extension of the TAZ for different GWHP injection regimes. Surface ERT could be used as a control tool for monitoring the successful functioning of GWHP in operation.

However, the sensitive analysis we performed show that the ERT sensitivity to the plume decreases strongly with the plume depth and depends also on its dimension. Thus, the qualitative characterization of the TAZ performed through ERT inversion is strongly influenced by the TAZ depth. Indeed, the method struggles to provide the shape of the TAZ in the lower part of the aquifer. In our case, most of the TAZ is really shallow, reaching the groundwater table 3 m deep, so the method is sensitive to changes induced in the subsurface by the TAZ development. Nevertheless, for a deeper TAZ, the electrode design should be adapted to explore the medium at greater depths. This can be done by using a larger distance between electrodes but at the cost of a lower spatial resolution.

Acknowledgments

The work by Nolwenn Lesparre was supported by the project SUITE4D from a BEcome a WAlloon REsearcher fellowship fund co-financed by the Department of Research Programs of the Federation Wallonia – Brussels and the COFUND program of the European Union. The field experiments was made possible thanks to the F.R.S.-FNRS research credit 4D Thermography, grant number J.0045.16. We gratefully acknowledge Thomas Kremer and Solomon Ehosioke who participated to the field works and data acquisition supervision.

Appendix A.1 Data analysis and error model

We assume that the data (resistance measurements) are uncertain due to noise and that the latter is composed of a random component and a systematic one correlated over time. The effect of systematic error, including modeling errors, can be canceled out by subtraction when working with data-differences inversion (LaBrecque and Yang, 2001). The weighting factors ϵ_B and ϵ_{TL} for the background and time-lapse inversions have to be correctly evaluated. As suggested by Slater et al. (2000) and Lesparre et al. (2017), we use the analysis of normal to reciprocal disparities. First,

resistance data were sorted to remove outliers and the data were selected so they presented a repetitive error lower than 1% and a reciprocal error lower than 5% for each time step. The total number of filtered data at each time step was reduced from 3045 to 1948 measurements.

For the background image, an error model ϵ_B was fit to the measured difference $|R_N - R_R|$ between the normal R_N and reciprocal resistance R_R after removing outliers and bining by $\langle R \rangle$. The errorϵ_B varies linearly with resistance (Fig. A.1 a, Slater et al., 2000):

$$\epsilon_B = a_B + b_B \langle R \rangle,$$

Equation A.1

with

$$\langle R_i \rangle = \frac{(R_{N,i} + R_{R,i})}{2} \text{ for all } i \text{ where } \frac{|R_{N,i} - R_{R,i}|}{\langle R_i \rangle} < 0.05 \, .$$

Equation A.2

For the estimate of an error model of the time lapse inversions, normal and reciprocal data at a given time were compared to the background measurements (Lesparre et al., 2017). The normal difference between times t_0 and t_i as $\Delta log R_N = log R_{N,i} - log R_{N,0}$, and the reciprocal difference as $\Delta log R_R = log R_{R,i} - log R_{R,0}$ were used in the time lapse inversions because the data fit were in the logarithmic domain. The difference error model ϵ_{TL} was then fit to the measured value of the normal-reciprocal discrepancy $|\Delta log R_N - \Delta log R_R|$ that varies linearly with the inverse of the resistance (Fig. A.1 b, Lesparre et al., 2017):

$$\epsilon_{TL} = a_{TL} + \frac{b_{TL}}{\langle R \rangle}$$

Equation A.3

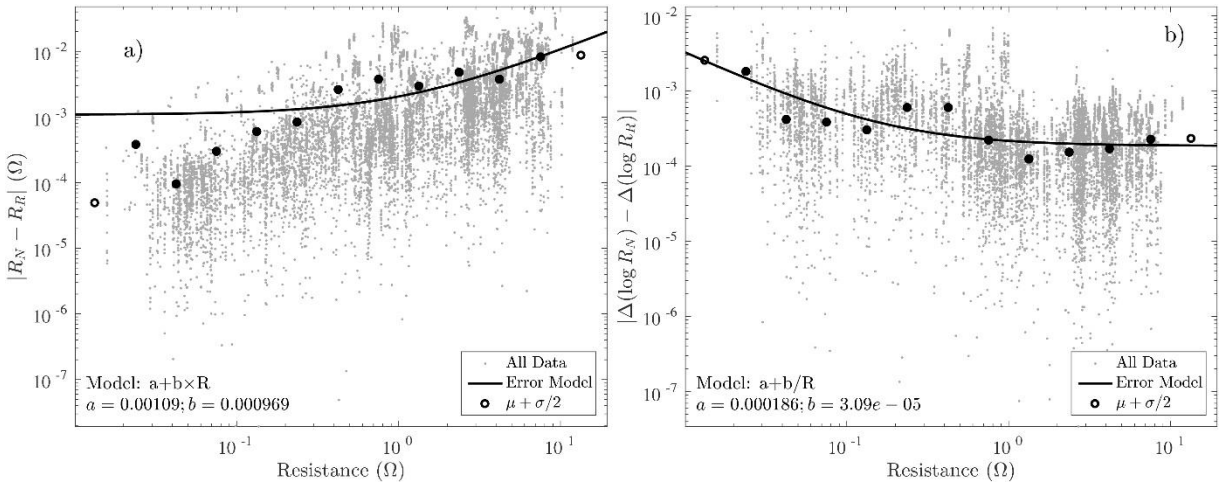

Figure A.1: Measured and model error from the normal and reciprocal acquisition for the background (a) and the time-lapse (b) inversions.

The error model parameters a_B, b_B, a_{TL} and b_{TL} were estimated by fitting the measured errors as a function of $\langle R \rangle$ (Fig. A.1). For the time-lapse error estimate, $\langle R \rangle$ also expresses as stated in Eq. A.2. Error data were divided into classes of $\langle R \rangle$ with four bins per decade of $\overline{R_i}$, logarithmically equally spaced. For each bin the average μ and the standard deviation σ were estimated (Koestel et al., 2008). The choice of the error threshold on which the error model is fitted impacts the data weighting and so the residuals χ that are used as a stopping criteria (see Eq. 5). We choose to fit both error models to $\mu + \sigma/2$ (Fig. A.1) in order to be more sensitive to conductivity variations due to the hot water injection.

References

Adler, A., Boyle, A., Crabb, M.G., Gagnon, H., Grychtol, B., Lesparre, N., Lionheart, W.R., 2015. EIDORS Version 3.8. In Proc. of the 16th Int. Conf. on Biomedical Applications of Electrical Impedance Tomography.

Allen, A., Milenic, D., 2003. Low-enthalpy geothermal energy resources from groundwater in fluvioglacial gravels of buried valleys. Appl. Energy 74, 9–19, http://dx.doi.org/10.1016/S0306-2619(02)00126-5.

Ampofo, F., Maidment, G.G., Missenden, J.F., 2006. Review of groundwater cooling systems in London. Appl. Therm. Eng., 26(17), 2055-2062, http://dx.doi.org/10.1016/j.applthermaleng.2006.02.013.

Ausseur, J.Y., Menjoz, A., Sauty, J.P., 1982. Stockage couplé de calories et de frigories en aquifère par doublet de forages. J. Hydrol., 56(3), 175-200, http://dx.doi.org/10.1016/0022-1694(82)90012-9.

Banks, D., 2009. Thermogeological assessment of open-loop well-doublet schemes: a review and synthesis of analytical approaches. Hydrogeol. J., 17(5), 1149-1155, http://dx.doi.org/10.1007/s10040-008-0427-6.

Bertermann, D., Bialas, C., Rohn, J., 2013. ThermoMap — area mapping of superficial geothermic resources by soil and groundwater data. Available at http://geoweb2.sbg.ac.at/thermomap/.

Bonte, M., van Breukelen, B.M., Stuyfzand, P.J., 2013. Temperature-induced impacts on groundwater quality and arsenic mobility in anoxic aquifer sediments used for both drinking water

and shallow geothermal energy production. Water Res., 47(14), 5088-5100, http://dx.doi.org/10.1016/j.watres.2013.05.049.

Bridger, D.W., Allen, D.M., 2014. Influence of geologic layering on heat transport and storage in an aquifer thermal energy storage system. Hydrogeol. J., 22(1), 233-250, http://dx.doi.org/10.1007/s10040-013-1049-1.

Brouyère, S., (Ph.D. thesis), 2001. Etude et modélisation du transport et du piégeage des solutés en milieu souterrain sariablement saturé. University of Liege (unpublished).

Cultrera, M., Boaga, J., Di Sipio, E., Dalla Santa, G., De Seta, M., & Galgaro, A., 2017. Modelling an induced thermal plume with data from electrical resistivity tomography and distributed temperature sensing: a case study in northeast Italy, Hydrogeol. J., 1-15. http://dx.doi.org/10.1007/s10040-017-1700-3

Caterina, D., Beaujean, J., Robert, T., Nguyen, F., 2013. A comparison study of different image appraisal tools for electrical resistivity tomography. Near Surf. Geophys., 11(6), 639-657, http://dx.doi.org/10.3997/1873-0604.2013022.

Dassargues, A., 1997. Modeling baseflow from an alluvial aquifer using hydraulic-conductivity data obtained from a derived relation with apparent electrical resistivity. Hydrogeol. J., 5(3), 97-108, http://dx.doi.org/:10.1007/s100400050125.

Derouane, J., Dassargues, A., 1998. Delineation of groundwater protection zones based on tracer tests and transport modeling in alluvial sediments. Environ. Geol., 36(1–2), 27–36, http://dx.doi.org/10.1007/s002540050317.

de Paly, M., Hecht-Méndez, J., Beck, M., Blum, P., Zell, A., Bayer, P., 2012. Optimization of energy extraction for closed shallow geothermal systems using linear programming. Geothermics 43, 57–65, http://dx.doi.org/10.1016/j.geothermics.2012.03.001.

European Council, 2012. Directive 2012/27/EU of the European Parliament and of the Council of 25 October 2012 on energy efficiency, amending Directives 2009/125/EC and 2010/30/EU and repealing Directives 2004/8/EC and 2006/32/EC. *Official Journal of the European Union*, Legislative acts. Brussels, Belgium.

731 Fiandaca, G., Doetsch, J., Vignoli, G., & Auken, E., 2015. Generalized focusing of time-lapse
732 changes with applications to direct current and time-domain induced polarization inversions.
733 Geophys. J. Int., 203(2), 1101-1112.

734 Galgaro, A., Cultrera, M., 2013. Thermal short circuit on groundwater heat pump. Appl. Therm. Eng.,
735 57(1), 107-115, http://dx.doi.org/10.1016/j.applthermaleng.2013.03.011.

736 Giordano, N., Comina, C., Mandrone, G., 2016. Laboratory scale geophysical measurements aimed
737 at monitoring the thermal affected zone in Underground Thermal Energy Storage (UTES)
738 applications. *Geothermics, 61,* 121-134, http://dx.doi.org/10.1016/j.geothermics.2016.01.011.

739 Giordano, N., Arato, A., Comina, C., Mandrone, G., 2017. Time-lapse electrical resistivity imaging
740 of the thermally affected zone of a Borehole Thermal Energy Storage system near Torino (Northern
741 Italy). J. Appl. Geophys., 140, 123-134, http://dx.doi.org/10.1016/j.jappgeo.2017.03.015.

742 Graf, T., Therrien, R., 2005. Variable-density groundwater flow and solute transport in porous media
743 containing nonuniform discrete fractures. Adv. water resour., 28(12), 1351-1367,
744 http://dx.doi.org/10.1016/j.advwatres.2005.04.011.

745 Griebler, C., Brielmann, H., Haberer, C. M., Kaschuba, S., Kellermann, C., Stumpp, C., Hegler F.,
746 Kuntz, D., Walker-Hertkorn, S., Lueders, T., 2016. Potential impacts of geothermal energy use and
747 storage of heat on groundwater quality, biodiversity, and ecosystem processes. Environ. Earth Sci.,
748 75(20), 1391, http://dx.doi.org/10.1007/s12665-016-6207-z.

749 Gringarten, A.C., Sauty, J.P., 1975. A theoretical study of heat extraction from aquifers with uniform
750 regional flow. J. Geophys. Res., 80(35), 4956-4962, http://dx.doi.org/10.1029/jb080i035p04956.

751 Haehnlein S., Bayer P., Blum P., 2010. International legal status of the use of shallow geothermal
752 energy. Renew. Sust. Energ. Rev., 14(9), 2611-2625, http://dx.doi.org/10.1016/j.rser.2010.07.069.

753 Hausner, M.B., Suárez, F., Glander, K.E., Giesen, N.V.D., Selker, J.S., Tyler, S.W., 2011. Calibrating
754 single-ended fiber-optic Raman spectra distributed temperature sensing data. Sensors, 11(11),
755 http://dx.doi.org/10859-10879 10.3390/s111110859.

756 Hayley, K., Bentley, L.R., Gharibi, M., Nightingale, M., 2007. Low temperature dependence of
757 electrical resistivity: Implications for near surface geophysical monitoring. Geophys. Res. Lett.,
758 34(18), http://dx.doi.org/10.1029/2007gl031124.

759 Hermans, T., Vandenbohede, A., Lebbe, L., Nguyen, F., 2012. A shallow geothermal experiment in
760 a sandy aquifer monitored using electric resistivity tomography. Geophysics 77(1), B11–B21,
761 http://dx.doi.org/10.1190/GEO2011-0199.1.

762 Hermans, T., Nguyen, F., Robert, T., Revil, A., 2014. Geophysical methods for monitoring
763 temperature changes in shallow low enthalpy geothermal systems. Energies, 7(8), 5083-5118,
764 http://dx.doi.org/10.3390/en7085083.

765 Hermans T., Wildemeersch S., Jamin P., Orban P., Brouyère S., Dassargues A., Nguyen F., 2015.
766 Quantitative temperature monitoring of a heat tracing experiment using cross-borehole ERT.
767 Geothermics, 53, 14–26, http://dx.doi.org/10.1016/j.geothermics.2014.03.013.

768 Hermans, T., Oware, E., Caers, J., 2016a. Direct prediction of spatially and temporally varying
769 physical properties from time-lapse electrical resistance data. Water Resour. Res., 52(9), 7262-7283,
770 http://dx.doi.org/10.1002/2016WR019126.

771 Hermans, T., Kemna, A., Nguyen, F., 2016b. Covariance-constrained difference inversion of time-
772 lapse electrical resistivity tomography data. Geophysics, 81(5), E311-E322,
773 http://dx.doi.org/10.1190/GEO2015-0491.1.

774 Hermans, T., Irving, J. 2017. Facies discrimination with electrical resistivity tomography using a
775 probabilistic methodology: effect of sensitivity and regularisation. Near Surface Geophysics, 15, 13-
776 25, http://dx.doi.org/10.3997/1873-0604.2016047.

777 Hermans, T., Nguyen, F., Klepikova, M., Dassargues, A., Caers, J. 2018. Uncertainty quantification
778 of medium-term heat storage from short-term geophysical experiments using Bayesian Evidential
779 Learning. Water Resources Research, in press, http://dx.doi.org/10.1002/2017WR022135.

780 Jesußek, A., Grandel, S., Dahmke, A., 2013. Impacts of subsurface heat storage on aquifer
781 hydrogeochemistry. Environ. Earth Sci., 69(6), 1999-2012, http://dx.doi.org/10.1007/s12665-012-
782 2037-9.

783 Kemna, A., 2000, Tomographic inversion of complex resistivity: theory and application. PhD Thesis.
784 University of Bochum.

785 Klepikova, M., Wildemeersch, S., Hermans, T., Jamin, P., Orban, P., Nguyen, F., Brouyère, S.
786 Dassargues, A., 2016. Heat tracer test in an alluvial aquifer: field experiment and inverse modelling.
787 J. Hydrol., 540, 812-823, http://dx.doi.org/10.1016/j.jhydrol.2016.06.066.

Koestel J., Kemna A., Javaux M., Binley A., Vereecken H. 2008. Quantitative imaging of solute transport in an unsaturated and undisturbed soil monolith with 3D ERT and TDR. Water Resour. Res., 44, W12411, http://dx.doi.org/0.1029/2007WR006755.

LaBrecque D.J., Miletto M., Daily W., Ramirez A., Owen E., 1996. The effects of noise on Occam's inversion of resistivity tomography data. Geophysics, 61(2), 538-548, http://dx.doi.org/10.1190/1.1443980.

LaBrecque, D.J., Yang, X. 2001. Difference inversion of ERT data: a fast inversion method for 3-D in-situ monitoring: J. Environ. Eng. Geoph., 6(2), 83-89, http://dx.doi.org/10.4133/JEEG6.2.83.

Lesparre, N., Nguyen, F., Kemna, A., Robert, T., Hermans, T., Daoudi, M., Flores-Orozco, A., 2017. A new approach for time-lapse data weighting in ERT. Geophysics, 82(6), 1-35, http://dx.doi.org/10.1190/geo2017-0024.1.

Liang, J., Yang, Q., Liu, L., Li, X., 2011. Modeling and performance evaluation of shallow ground water heat pumps in Beijing plain, China. Energy Buildings, 43, 3131–3138, http://dx.doi.org/10.106/j.enbuild.2011.08.007.

Lo Russo, S., Civita, M.V., 2009. Open-loop groundwater heat pumps development for large buildings: a case study. Geothermics 38, 335–345, http://dx.doi.org/10.1016/j.geothermics.2008.12.009.

Lo Russo, S. L., Boffa, C., Civita, M. V., 2009. Low-enthalpy geothermal energy: an opportunity to meet increasing energy needs and reduce CO 2 and atmospheric pollutant emissions in Piemonte, Italy. Geothermics, 38(2), 254-262, http://dx.doi.org/10.1016/j.geothermics.2008.07.005.

Lo Russo, S. L., Gnavi, L., Roccia, E., Taddia, G., Verda, V., 2014. Groundwater Heat Pump (GWHP) system modeling and Thermal Affected Zone (TAZ) prediction reliability: Influence of temporal variations in flow discharge and injection temperature. Geothermics, 51, 103-112, http://dx.doi.org/10.1016/j.geothermics.2012.02.001.

Mattsson, N., Steinmann, G., Laloui, L., 2008. Advanced compact device for the in situ determination of geothermal characteristics of soils. Energy Buildings, 40, 1344–1352, http://dx.doi.org/10.1016/j.enbuild.2007.12.003.

Milnes, E., Perrochet, P., 2013. Assessing the impact of thermal feedback and recycling in open-loop groundwater heat pump (GWHP) systems: a complementary design tool. Hydrogeol. J., 21(2), 505-514, http://dx.doi.org/10.1007/s10040-012-0902-y.

Nguyen, F., Kemna, A., Robert, T., & Hermans, T., 2016. Data-driven selection of the minimum-gradient support parameter in time-lapse focused electric imaging. Geophysics, 81(1), A1-A5, http://dx.doi.org/10.1190/GEO2015-0226.1.

Nimmer, R.E., Osiensky, J.L., Binley, A.M., Williams, B.C., 2008. Three-dimensional effects causing artifacts in two-dimensional, cross-borehole, electrical imaging. J. Hydrol., 359(1), 59-70, http://dx.doi.org/10.1016/j.jhydrol.2008.06.022.

Pollock, D., Cirpka, O.A., 2012. Fully coupled hydrogeophysical inversion of a laboratory salt tracer experiment monitored by electrical resistivity tomography. Water Resour. Res., 48(1), http://dx.doi.org/10.1029/2011WR010779.

Polydorides, N., Lionheart, W.R., 2002. A Matlab toolkit for three-dimensional electrical impedance tomography: a contribution to the Electrical Impedance and Diffuse Optical Reconstruction Software project. Meas. Sci. Technol., 13(12), 1871, http://dx.doi.org/10.1088/0957-0233/13/12/310.

Possemiers, M., Huysmans, M., Batelaan, O., 2015. Application of multiple-point geostatistics to simulate the effect of small-scale aquifer heterogeneity on the efficiency of aquifer thermal energy storage. Hydrogeology Journal 23, 971–981, http://dx.doi.org/10.1007/s10040-015-1244-3.

Raymond, J., Therrien, R., Gosselin, L., Lefebvre, R., 2011. A review of thermal response test analysis using pumping test concepts. Ground Water, 49, 932–945, http://dx.doi.org/10.1111/j.1745-6584.2010.00791.x.

Rein, A., Hoffmann, R., Dietrich, P., 2004. Influence of natural time-dependent variations of electrical conductivity on DC resistivity measurements. J. Hydrol., 285(1), 215-232, http://dx.doi.org/10.1016/j.jhydrol.2003.08.015.

Revil, A., Cathles, L.M., Losh, S., Nunn, J.A., 1998. Electrical conductivity in shaly sands with geophysical applications. J. Geophys. Res., 103(B10), 23925-23936, http://dx.doi.org/10.1029/98jb02125.

Rucker, D.F., 2014. Investigating motion blur and temporal aliasing from time-lapse electrical resistivity: J. Appl. Geophys., 111, 1-13, http://dx.doi.org/10.1016/j.jappgeo.2014.09.010.

844 Sarbu, I., Sebarchievici, C., 2014. General review of ground-source heat pump systems for heating
845 and cooling of buildings. Energy and buildings, 70, 441-454, http://dx.doi.org/10.5772/61372.

846 Singha, K., Moysey, S., 2006. Accounting for spatially variable resolution in electrical resistivity
847 tomography through field-scale rock-physics relations. Geophysics, 71(4), A25-A,
848 http://dx.doi.org/2810.1190/1.2209753.

849 Singha, K., Day-Lewis, F.D., Johnson, T., Slater, L.D., 2015. Advances in interpretation of
850 subsurface processes with time-lapse electrical imaging. Hydrol. Proc., 29(6), 1549-1576,
851 http://dx.doi.org/10.1002/hyp.10280.

852 Slater L., Binley, A.M., Daily W., Johnson, R., 2000. Cross-hole electrical imaging of a controlled
853 saline tracer injection. J. Appl. Geophys., 44, 85-102, http://dx.doi.org/10.1016/S0926-
854 9851(00)00002-1.

855 Sommer, W., Valstar, J., van Gaans, P., Grotenhuis, T., Rijnaarts, H., 2013. The impact of aquifer
856 heterogeneity on the performance of aquifer thermal energy storage: Water Resources Research 49,
857 8128–8138, http://dx.doi.org/10.1002/2013WR013677.

858 Sommer, W.T., Doornenbal, P.J., Drijver, B.C., van Gaans, P.F.M., Leusbrock, I., Grotenhuis, J.T.C.,
859 Rijnaarts, H.H.M., 2014. Thermal performance and heat transport in aquifer thermal energy storage.
860 Hydrogeology Journal 22, 263–279, http://dx.doi.org/10.1007/s10040-013-1066-0.

861 Therrien, R., McLaren, R.G., Sudicky, E.A., Panday, S.M., 2010. HydroGeoSphere: a three-
862 dimensional numerical model describing fully-integrated subsurface and surface flow and solute
863 transport. *Groundwater Simulations Group, University of Waterloo, Waterloo, ON*.

864 Tikhonov, A. 1963. Solution of incorrectly formulated problems and the regularization method.
865 Soviet Meth. Dokl., 4, 1035-1038.

866 Van Hoorde, M., Hermans, T., Dumont, G., Nguyen, F. 2017. 3D electrical resistivity tomography of
867 karstified formations using cross-line measurements. Engineering Geology, 230, 123-132,
868 http://dx.doi.org/10.1016/j.enggeo.2017.01.028.

869 Vanhoudt, D., Desmedt, J., Van Bael, J., Robeyn, N., Hoes, H., 2011. An aquifer thermal storage
870 system in a Belgian hospital: Long-term experimental evaluation of energy and cost savings. Energy
871 and Buildings, 43(12), 3657-3665, http://dx.doi.org/10.1016/j.enbuild.2011.09.040.

872 Voigt, H.D., Haefner, F., 1987. Heat transfer in aquifers with finite caprock thickness during a thermal
873 injection process. Water Resour. Res., 23(12), 2286-2292,
874 http://dx.doi.org/10.1029/wr023i012p02286.

875 Wildemeersch, S., Jamin, P., Orban, P., Hermans, T., Klepikova, M., Nguyen, F., Brouyère, S.,
876 Dassargues, A., 2014. Coupling heat and chemical tracer experiments for estimating heat transfer
877 parameters in shallow alluvial aquifers. J. Contam. Hydrol., 169, 90-99,
878 http://dx.doi.org/10.1016/j.jconhyd.2014.08.001.